Electrochemical Investigation of Molten Lanthanum-Yttrium Oxide for Selective Liquid Rare-Earth Metal Extraction

Citation: Nakanishi, Bradley R. and Antoine Allanore. "Electrochemical Investigation of Molten Lanthanum-Yttrium Oxide for Selective Liquid Rare-Earth Metal Extraction." Journal of The Electrochemical Society, 166, 13 (September 2019): E420-E428 © 2019 The Author(s)

As Published: 10.1149/2.1141913JES

Publisher: The Electrochemical Society

Persistent URL: https://hdl.handle.net/1721.1/127225

Version: Final published version: final published article, as it appeared in a journal, conference proceedings, or other formally published context

Electrochemical Investigation of Molten Lanthanum-Yttrium Oxide for Selective Liquid Rare-Earth Metal Extraction

Electrochemical Investigation of Molten Lanthanum-Yttrium Oxide for Selective Liquid Rare-Earth Metal Extraction

Bradley R. Nakanishi and Antoine Allanore [z]

Department of Materials Science and Engineering, Massachusetts Institute of Technology, Cambridge, Massachusetts 02139, USA

The electrochemical separation of lanthanum from yttrium as liquid metal is investigated starting from their molten mixture as sesquioxides, La_2O_3 and Y_2O_3, at temperature in excess of 2500K. Using iridium electrodes, a combination of dc and ac electrochemical methods and a thermal imaging furnace, the selectivity for liquid rare-earth metal recovery is evaluated for 6 compositions across the pseudo-binary La_2O_3 - Y_2O_3. Departure from the thermodynamic predictions based on ideal mixture for the molten rare-earth oxides and their alloy is experimentally demonstrated, with selectivity several order of magnitude different than the standard state predictions. A critical assessment of a possible model for the thermodynamic of mixing is presented to describe the non-ideal mixing behavior for the pseudo-binary La_2O_3 - Y_2O_3. The selective enrichment observed using molten rare-earth electrolysis suggests a possible new approach for direct, selective, REE separation and recovery.
 [DOI: 10.1149/2.1141913jes]

Manuscript submitted June 25, 2019; revised manuscript received August 5, 2019. Published September 6, 2019.

The rare earth elements (REE) are the group containing the lanthanides plus scandium and yttrium. Catalysts, ceramics, glass-polishing products represent the largest market for rare-earth oxides (REO), where often a pure REO is the precursor for each product. In the last 20 years, rare-earth metals have also found critical use in emerging high tech markets due to their unique electromagnetic properties. The demand for REE is expected to continue to grow significantly in part due to their applications in renewable power generation and usage. Usually, those applications utilize a single REE as an alloying element or as constituent of an active compound. Overall, rare-earth elements are commercialized in their pure form either as compound or metal. However they are mined from natural mineral phases that contain all REE, though their relative proportion in the mineral may vary.[1] REE usage therefore calls for both mining and separation, the later being challenging due to the similar chemistry of those elements.

The REE market exhibits the so-called "balance problem".[2] Market values presented in Table I drastically increase, on a metal basis, from rare earth oxide concentrate to pure REO and pure REE, though differences are noticeable. Value increases from concentrate to metal by around 3x for a major REO concentrate component like lanthanum (23% of a concentrate of the mineral bastnäsite is lanthanum). However, the value of yttrium, with 2% content in the concentrate, increases by nearly 200x in its metal form. The situation is even more drastic for minor REE like dysprosium, with nearly 100,000x increase in value from concentrate to metal, with a content in the concentrate only 1000x lower than lanthanum. Such trends arise from the process and economic challenges of this industry, signaling the critical need for new separation techniques that are selective to one or several rare-earth elements from the concentrate.

Current industrial-scale technologies from concentrate to metal rely on a complex sequence of hydrometallurgical processes involving solvent extraction,[3,4] taking advantage of the slight differences in chemical bonding exacerbated in organic solvents. However, because separation factors between individual REE range between 1 and 5,[5,6] repeated cycling and solvent regeneration, along with sequential REE separation is often necessary. After stripping, recovery, precipitation, calcination, and chlorination or fluorination, REE halides compounds are typically electrowon if metal is the target product.

Limitations of the present supply chain, beyond geopolitics, include intensity of capital, labor, hazardous chemicals and expensive liquid solvents handling.[7] Several alternative methods have been proposed for selective REE extraction, such as combined selective reduction and vacuum distillation in chlorides.[8] However, no methods have been reported to date that involve processing in solvents solely composed of oxides. Operating an oxide-based solvent is attractive from a minerals processing standpoint, as the production of REO concentrate containing up to +90% REO can be achieved with physical separation and several possible leaching processes can separate the remaining silicates.[9] Producing a concentrate mixed oxide with proportions in REE relatively close to the mineral phase is therefore possible, and has a market value that is relatively well identified, at around $10 per kilogram.

Starting from a concentrate of mix REO, the challenge of separation is two-fold. First, REO have limited solubility in low-temperature solvents, and melting points higher than 2500K (see Table II). Second, rare-earth oxides exhibit broad miscibility in the liquid state, as illustrated in Figure 1 with the pseudo-binary phase diagram for sesquioxides of lanthanum (lanthania, La_2O_3) and yttrium (yttria, Y_2O_3). An additional driving force for separation is likely needed to recover one or several REE from molten rare-earth oxides. Electrolysis is a proven candidate for separation, where electrons can function as the reductant and may provide a high degree of selectivity for the production of metal or alloys. This principle has been put forth for spent nuclear fuel treatment methods, for the separation of actinides and lanthanides, for example in molten halides[10] or fluorides.[11] With the recent successful demonstration of molten oxide electrolysis in molten aluminium oxide (T>2300K) to produce liquid aluminium and oxygen,[12] it is herein proposed to evaluate the feasibility of molten rare-earth sesquioxides

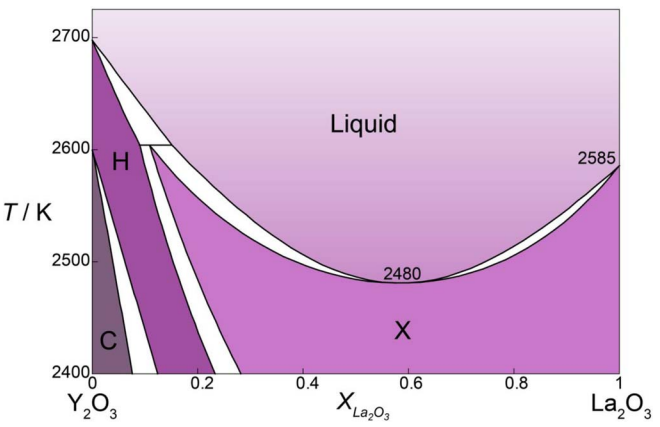

Figure 1. High-temperature region of the pseudo-binary La_2O_3-Y_2O_3 phase diagram, calculated via the recent thermodynamic assessment by Chen et al.[32] using FactSage.[50] Phases shown include the liquid and the high temperature solid solution phases (hexagonal H-phase and cubic X- and C-phases).

[z]E-mail: allanore@mit.edu

Table I. Metal value per kg of products for lanthanum, dysprosium and yttrium from mining concentrate to pure metal.

Metal Market Value in ($) per kg of product	La_2O_3 (85% La)	Dy_2O_3 (87% Dy)	Y_2O_3 (79% Y)
Bastnasite concentrate (metal content)	2 (23%)	0.0009 (0.01%)	0.19 (2.1%)
Oxide (value increase vs concentrate)	2.8 (x1.3)	199 (x220945)	4.2 (x22)
Metal (value increase vs concentrate)	5.5 (x2.7)	246 (x273333)	37 (x196)

Typical bastnäsite concentrate metal content (in wt%): Ce: 45, La: 23, Nd: 18, Pr: 5, Sm: 3.5, Y: 2.1, Gd: 1.8, Er: 1, Eu: 0.1, Yb, Tm, Lu, Dy, Ho, Tb: 0.01, Sc: 0.001

Concentrate, pure oxide and pure metal estimates from USGS 2019 Minerals Yearbook and Rare Metal News (Japan) No. 2834 published on 2/8/2019

(M_2O_3) electrolysis to produce liquid rare-earth metal (M) and oxygen, following Reaction 1:

$$M_2O_3\ (l) \rightleftharpoons 2M\,(l) + {}^3/_2O_2(g) \quad [1]$$

Considering metal electrochemical separation from a molten mixture of sesquioxides, the selectivity for a given element can be defined following the stoichiometry of Reaction 1:

$$D = \frac{(x_M)^2}{X_{M_2O_3}} \quad [2]$$

where x_M is the molar (or weight) fraction of the element in the metal cathode product, and $X_{M_2O_3}$ is the molar (or weight) fraction of the element in the molten oxides. Selectivity is used to define a separation factor (S) between two elements, for example here M from N recovered in a mix metal cathode:

$$S = \frac{\frac{(x_M)^2}{X_{M_2O_3}}}{\frac{(x_N)^2}{X_{N_2O_3}}} \quad [3]$$

A separation factor greater than unity is the target, though its variation with the concentration of the elements in the electrolyte is also important for practical application. Selectivity can in principle be related to the thermodynamic equilibrium constant, and can be computed from partial molar Gibbs energy in both the electrolyte and cathode product, as a basis for comparison.

While some data have been provided for REE in halides for example,[10] they are not available nor can be computed for molten REO. In addition, no evidence of electrochemical recovery of REE from molten REO is available to date. We herein investigate the feasibility of such electrochemical recovery principles for the system La_2O_3-Y_2O_3, as well as the influence of the concentration of metal oxide in the electrolyte. As presented in Table II, lanthanum oxide in its standard state is around 160 mV easier to decompose to metal (per mole of oxygen gas) than yttrium oxide, which is one of the most stable rare-earth oxides. According to physical chemical data, the +3 valence is the only stable state for La and Y ions, and attempting selective separation of La from Y from their mixture as molten sesquioxide is therefore a reasonable first step.

For a pseudo binary molten mixture of oxides, the selectivity for La versus Y anticipated assuming ideal solution in both the electrolyte and metal product is computed using the equilibrium condition for the exchange reaction:

$$La_2O_3\ (l) + 2Y\,(l) \rightleftharpoons Y_2O_3\ (l) + 2La\,(l) \quad [4]$$

For a ideal binary metal product, and an ideal pseudo binary electrolyte, one can directly relates the content of one metal in the cathode (e.g. x_{La}) as a function of the equilibrium constant K and the metal oxide content in the electrolyte (e.g. $X_{La_2O_3}$), where activities (a_i) are equal to concentration:

$$K = e^{\frac{2\left(\mu^o_{La}-\mu^o_Y\right)+\mu^o_{Y_2O_3}-\mu^o_{La_2O_3}}{RT}} = \frac{(a_{La})^2}{a_Y{}^2}\frac{\left(a_{Y_2O_3}\right)}{a_{La_2O_3}} = \frac{(x_{La})^2}{x_Y{}^2}\frac{\left(X_{Y_2O_3}\right)}{X_{La_2O_3}}$$

$$= \frac{(x_{La})^2}{(1-x_{La})^2}\frac{1-X_{La_2O_2}}{X_{La_2O_2}} \quad [5]$$

At 2585K, using standard thermodynamic data reported in Table II, $K = 77$. Often in separation technology, S presented in Eq. 3 is defined as K from Eq. 5, i.e. using concentration instead of activity. This is a fair point of departure for rare-earth separation from their molten oxides, since the phase diagram for the pseudo-binary rare-earth oxides (e.g. La_2O_3-Y_2O_3 reproduced in Figure 1) are typically modeled using ideal mixing for the liquid phase. In addition, the liquid rare-earth metal binaries (here La - Y) are also conventionally modeled as ideal mixture. From such prior knowledge, one would predict the sole extraction and very selective extraction of La in the metal phase across all molten La_2O_3-Y_2O_3 compositions. However, in addition to the lack of evidence of electrochemical deposition of metal from such electrolyte, experimental evidences are lacking to confirm the mixing behavior in both the oxide and metal liquid phases.

Previously, we presented the thermodynamics evaluation of the unary-component, molten Al_2O_3 investigated using decomposition voltage measurements combined with AC voltametry in a thermal imaging furnace,[12] showing the production of liquid aluminium. Such an approach allows for direct measurement of Gibbs energy and chemical potential in ionic molten oxide melts. Herein, we extend this approach to the system La_2O_3-Y_2O_3. Rare-earth metal electrochemical production from molten rare-earth oxide is investigated. The implications of the experimental results with respect to rare-earth oxide stability for the selective recovery of rare-earth metal are discussed, along with the possible selective extraction via molten rare-earth electrolysis.

Experimental

The experimental methods are similar to those employed by Nakanishi et al.[12] Here, only relevant deviations from the previous experimental procedure are described.

Electrolyte compositions investigated.—Powders of yttrium and lanthanum oxides (both >99.9% purity, diameter ø < 10 μm, Alfa Aesar) were mixed to the compositions shown in Table III, formed

Table II. Selected properties for pure, molten La_2O_3 & Y_2O_3 near T_{fus}.[45–52]

	T_{fus} K	$\Delta_{fus}S^o$ J mol^{-1} K^{-1}	V_m cm^3 mol^{-1}	p_i^o Pa	σ Ω^{-1} cm^{-1}	E_g (T = 0 K) eV	$\Delta E^\circ = \frac{-\Delta_r G^\circ}{4F}$ (at 2585 K) V (per mole O_2)
La_2O_3	2574	30.3	n.a	12.4	n.a.	3.83	1.839
Y_2O_3	2712	30.9	21.7	1.2	18	4.45	2.001

Table III. Electrolyte compositions & approximate temperatures investigated.[13,46,47,53,54]

$X_{La_2O_3}$	T_{liq} K	T_{liq} + 50 K K
0	2712	2762
0.2	2594	2644
0.4	2523	2573
0.6	2491	2541
0.8	2507	2557
1	2574	2624

into rods, and sintered. Details regarding preparation of oxide sample rods are available in Ref. 12.

Electrochemical measurements and operation.—Wires of iridium (Ir >99.9%, Ø 0.5 mm, 20 mm length, Furuya Metals Co., Ltd.) were employed in a three-electrode cell composed of working (WE), counter (CE) and pseudo-reference (RE) electrodes. The RE consisted of an Ir wire immersed in the molten droplet and measured potentials are referred to this RE, unless stated otherwise.

One of three geometries was employed for the WE or CE: 1) a single Ir wire with an approximate geometric surface area (A_G) of 0.07 cm^2, 2) a single Ir wire that was approximately 2 mm longer (A_G = 0.13 cm^2), or 3) two Ir wires TIG-welded together at their tips forming a spherical junction (approximately 1 mm dia., A_G = 0.25 cm^2).

Open circuit potential (OCP), electrochemical impedance spectroscopy (EIS), direct current (DC) linear sweep voltammetry (LSV), large amplitude Fourier transform alternating-current voltammetry (ACV) and potentiostatic and galvanostatic electrolysis measurements were performed.

Details regarding molten pendant droplet formation, electrode insertion and operation utilizing a modified thermal imaging furnace (TIF, TX-12000-I-MIT-VPO-PC, Crystal Systems Corp.) are described elsewhere.[12] For each experimental trial, electrochemical measurements were performed at a single furnace lamp power (i.e. temperature), defined as the minimum lamp power required maintaining a fully molten droplet after electrode insertion, which was confirmed and monitored by EIS and OCP measurements. This temperature, presented in the third column of Table II, was estimated by adding 25 K superheat to either:

- The temperature of melting (T_{fus}) from Table I for $X_{La_2O_3}$ = 0 or 1, or
- the average liquidus temperature (T_{liq}) at $X_{La_2O_3}$ using the experimental results of Lopato et al.[13] and Coutures et al.,[14] rejecting those of Mizuno et al.[15]

One composition of argon gas (UHP Ar, >99.999% Ar, p_{O_2} around 1 Pa, Airgas Inc.) was employed in this study. A trace oxygen (O_2) gas sensor (model 2001RSM, Advanced Micro Instruments Inc., sensor calibrated with air) was connected to the furnace exhaust gas for O_2 concentration quantification. Further details of the equipment, measurement methods and operation are available in Reference 12.

Post-experiment observation and analysis.—The microstructure and composition of the post-quenched, sectioned and polished droplets and electrodes were analyzed using an optical microscope, scanning electron microscope (SEM), and electron probe micro-analyzer (EPMA, JXA-8200, JEOL Ltd.) equipped for wavelength dispersive X-ray spectroscopy (WDS). Further details regarding observations and analytical equipments are described in References 12, 17.

Results

ACV measurements for the anode and cathode.—A typical ACV voltammogram for $X_{La_2O_3}$ = 0.8 showing the dc component of cell voltage and current, as well as the current harmonics versus dc potential, is presented in Figure 2. For positive potentials, an electrode labeled "anode" served as a WE. A faradaic event was observed at $E = E_A^*$ and corresponding with the half-cell reaction between oxide ions O^{2-} in the melt and oxygen gas $O_2(g)$ at 1 atm given by:

$$O^{2-}\,(melt) \rightleftharpoons 2e^- + \frac{1}{2}O_2\,(g) \qquad [6]$$

For all $X_{La_2O_3}$ studied, the following observations confirmed the correspondence between E_A^* and Reaction 6:

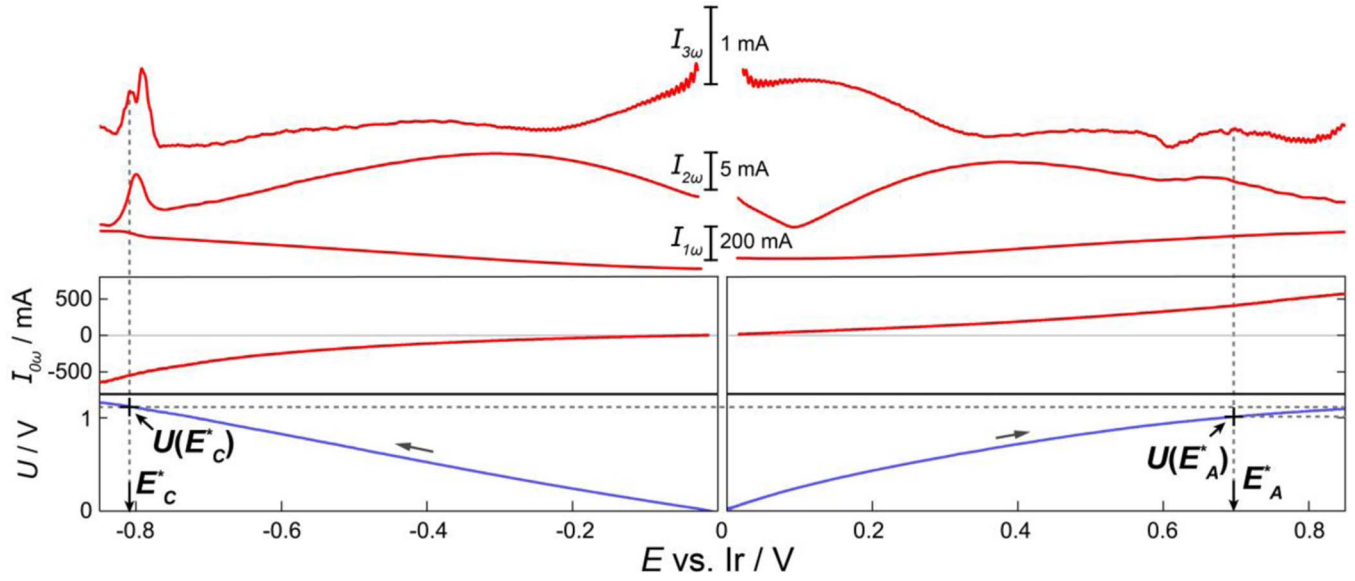

Figure 2. From bottom to top, dc component of cell voltage and dc, first, second and third harmonic current responses obtained during ACV measurements on an Ir WE in $X_{La_2O_3}$ = 0.8. To the left, for E < 0, is the cathode reaction study (cathode geometric surface area $A_{G,C}$ = 0.024 cm^2, applied dc potential scan limits −0.001 to −0.9 V vs. Ir); while to the right, for E > 0 is the anode reaction study (anode $A_{G,A}$ = 0.063 cm^2, +0.001 to +0.9 V vs. Ir). For both, E_{ac} = 150 mV, f = 23 Hz, υ = 20 mV s^{-1}. U was corrected for ohmic drop but not E ; $R_u(E = E_C^*) = 0.50\ \Omega$ and $R_u(E = E_A^*) = 0.47\ \Omega$. The quantities E_A^*, E_C^*, $U(E_A^*)$ and $U(E_C^*)$ are described in the text.

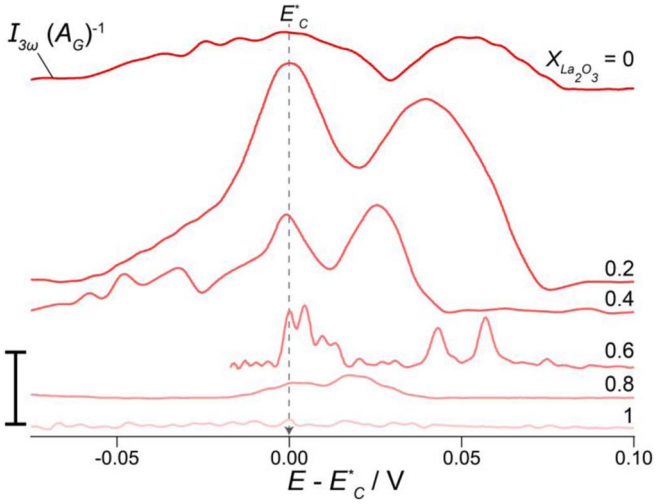

Figure 3. Variation of third harmonic of current during ACV measurements for an Ir cathode in La_2O_3-Y_2O_3 normalized by cathode geometric surface area versus $E - E^*_C$ (y-axis scale bar 50 mA cm^{-2}); signals are offset arbitrarily along the y-axis. For all: E_{ac} = 150 mV, f = 23 Hz and ν = 20 mV s^{-1}, negative-going scan. Again, E was not corrected for ohmic drop here to clarify interpretation.

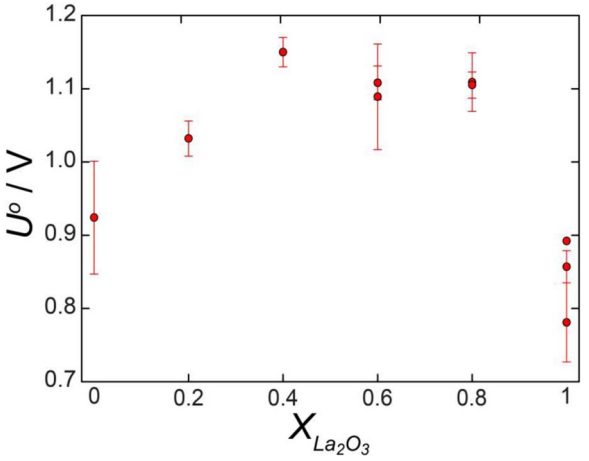

Figure 4. Variation of the measured U° versus mole fraction in La_2O_3. Error bars reflect one standard deviation (1σ) variation on repeated cathodic and anodic scans.

• Oxygen bubbling in the vicinity of the anode was always observed and detected by an oxygen sensor on the furnace exhaust line concomitant with the anode attaining electrode potential $E > E^*_A$.

• The similarity of peak-splitting features across 2nd and higher current harmonics with that observed for an Ir anode in molten Al_2O_3.[12]

• The relative stability of the Ir anode during the short-duration electrolysis

The features for the ACV voltammogram for an Ir anode were found to be consistent for all $X_{La_2O_3}$ investigated, permitting detection and measurement of the electrochemical reaction potential E^*_A coinciding with Reaction 6.

The features for the ACV voltammogram for an Ir cathode were found to be qualitatively similar in shape for all $X_{La_2O_3}$ investigated as presented for $I_{3\omega}$ in Figure 3, permitting detection and measurement of the electrochemical reaction potential E^*_C. Two peaks were consistently observed and the more negative potential of these two peaks was identified as E^*_C. The intensity normalized by geometric surface area was greatest for $X_{La_2O_3} = 0.2$ and decreased as $X_{La_2O_3} \to 1$.

Decomposition voltage measurements.—ACV measurements were performed with simultaneous measurement of the cell voltage (U). The value of U coinciding with E^*_A is designated as $U(E^*_A)$. A similar description relates E^*_C and $U(E^*_C)$. Similarly to that described by Nakanishi et al.,[12] the relative values of $U(E^*_C)$ and $U(E^*_A)$ were found to vary with cell geometry, i.e. the relative geometric surface areas of cathode and anode. The value of $U(E^*_C)$ which satisfied $U(E^*_C) > U(E^*_A)$ will hereafter be denoted as U^o. In practice, $U(E^*_C)$ was generally found to be greater than $U(E^*_A)$, when the cathode to anode immersed area ratio ($A_{G,C}/A_{G,A}$) was greater than 1.5 for all $X_{La_2O_3}$ for the conditions investigated.

The variation of U^o with $X_{La_2O_3}$ was found to increase from $X_{La_2O_3} = 0$ to 0.4 and subsequently decreased to $X_{La_2O_3} = 1$, as presented in Figure 4. Identification of half-cell reactions corresponding with E^*_C and $U(E^*_C)$ on the cathode were further investigated using electrolysis.

Electrolysis.—Electrolysis of molten La_2O_3-Y_2O_3 droplets was performed using three Ir electrodes to determine the half-cell reactions occurring on cathode corresponding with E^*_C and $U(E^*_C)$. Representative electrochemical signals and oxygen partial pressure in the furnace exhaust gas stream during electrolysis in La_2O_3-Y_2O_3 are presented in Figure 5. Bubbling was observed in the vicinity of the anode, which was confirmed to be oxygen gas from the oxygen sensor. The droplet and electrodes were quenched after electrolysis by shutting off the furnace lamps.

For all electrolyte compositions investigated, post experimental analyses of polished cross-sections of the droplet and electrodes showed that the conditions of the reference electrode and anode following electrolysis, and for all electrodes prior to electrolysis were visually unchanged. However, small particles (ø < 1 μm) were observed in the electrolyte bulk. Exact compositions for the particles were difficult to determine by WDS given their small size. A similar observation for Ir particles in silicate melts at T = 1823 K has been reported by Kim et al.[18] For galvanostatic experiments at very large currents (I = 3 A) and short duration (60 s), the droplet surface next to the anode was more vigorously perturbed by gas bubbles. Additionally, the post-quenched electrolyte next to the anode was observed to be colored red-orange, but the Ir content was below the WDS detection limit and the shape of the Ir anode remained visually unchanged. These observations are likely explained by the anodic dissolution of Ir into the La_2O_3-Y_2O_3 melt at high current densities (>30 A cm^{-2}). Furthermore, thermodynamic considerations for the formation of IrO_x gaseous species under such conditions suggest that their total partial pressure is quite low (p_{IrO_x} < 100 Pa).[19] Therefore, considering oxygen and IrO_x vapor species only, the fraction of faradaic current driving oxygen gas evolution is approximately 10^4–10^5 times greater than that for Ir oxidation. Therefore, while sufficient to give a coloration upon solidification, the concentrations of Ir in both the gas phase and melt at the anode were negligibly small.

Typical polished cross-sections for the cathode following potentiostatic electrolysis at cell potential difference $U > U^o$ are shown in Figure 6 for the various electrolytes. For $X_{La_2O_3}$ = [0.2, 0.4, 0.6, 0.8], La and Y were observed to co-deposit. The solidified cathodic deposit contained at least two metallic alloy phases; one Ir-rich alloy phase with contents of La and Y below the WDS detection limit (<200 ppm) and a second alloy phase containing La-Y-Ir with total REE content greater than 20 mol%. Observations at macroscale (Figures 6a to 6f) and microscale (Figures 6g to 6l) reveal notable trends. The cathode shape was severely modified for $X_{La_2O_3} = 0$, presumably upon melting by Rayleigh instability effects. This deformation was not observed for other $X_{La_2O_3}$. For $X_{La_2O_3} \neq 1$, large cavities (equivalent diameter of around 100 μm) were observed. At the electrode-electrolyte interface, oxide inclusions (equivalent diameter of less than 10 μm) formed within the metallic deposit. For $X_{La_2O_3} = 1$, La was not detected at the core of the electrode. For $X_{La_2O_3} \neq 1$, the internal bulk of the electrode contained the two alloy phases previously described. In

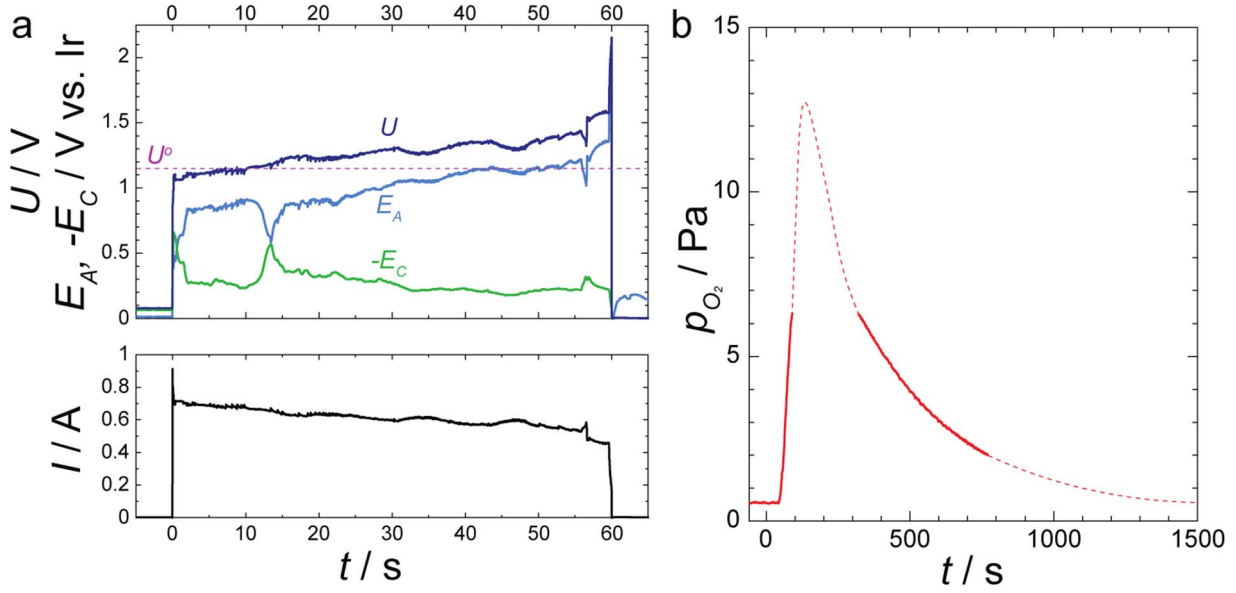

Figure 5. (a) Anode (E_A) and cathode ($-E_C$) potentials, cell voltage (U), current (I, bottom graph) and (b) detected oxygen partial pressure (p_{O_2}) during potentiostatic electrolysis at 2.5 V applied cell voltage; at $t = 60$ s, the lamps were shut off ($X_{La_2O_3} = 0.4$, $Q = 36.50$ C, $A_{G,C} = 0.02$ cm^2, $A_{G,A} = 0.01$ cm^2, gas flow rate = 50 cm^3 min^{-1}, T = 2573 K). For p_{O_2}, dashed lines represent extrapolated signal where either i) p_{O_2} exceeded sensor range (6.3 Pa) or ii) sensor recording was terminated.

particular, the La-Y-Ir phase adopts needle-like morphology. The Ir-rich phase was characterized by fine (equivalent diameter of less than 1 μm), interconnected particles forming a web-like structure; the former La-Y-Ir phase appearing to occur in a web of such Ir-rich particles. This microstructure relates to the solidification of the liquid cathode product. The La-Y-Ir phase found as a solid in the web of Ir-rich particles represents the remaining liquid present as the Ir-rich particles are precipitating. As such, the La-Y-Ir phase observed in the Ir-rich particles can be considered as a proxy to the liquid metal present at temperature.

The composition of the La-Y-Ir alloy phase was further characterized according to the chemical formula $(La_zY_{1-z})\,Ir_x$. The z parameter quantifies the relative fraction of La to Y in the Ir alloy phase based on an average of at least five WDS point analyses; and x represents

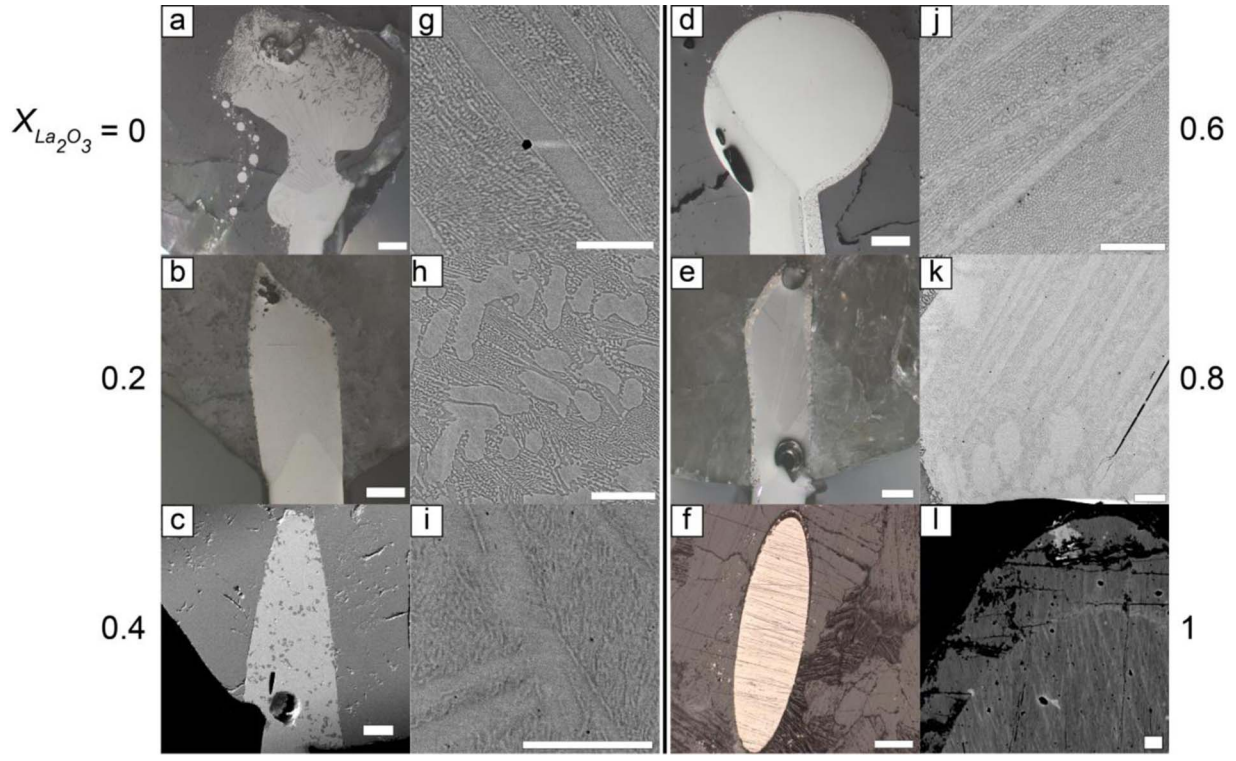

Figure 6. Micrographs of quenched cathode and droplet following potentiostatic electrolysis at cell potential $U > U^o$ for the investigated electrolyte compositions. Droplets quenched after 60 s of current flow. (a)-(b) and (d)-(f) are optical micrographs, and (c) is a secondary electron image (SEI), of the cathodes in the solidified electrolyte. (a)-(f) scale bar 200 μm; (g)-(l) are back-scatter electron (BEC) images of cathode deposit at higher magnification, (g)-(l) scale bar 10 μm.

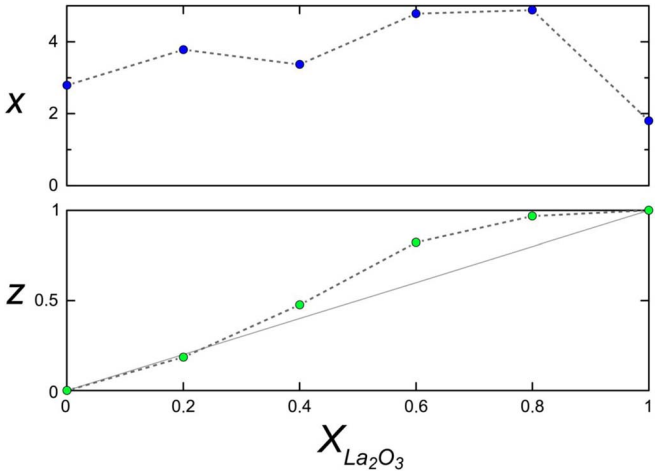

Figure 7. Variation of the cathode deposit composition versus $X_{La_2O_3}$. The composition parameters x and z are defined according to the chemical formula $(La_zY_{1-z})Ir_x$. x is the minimum and z is an average (uncertainty $1\sigma < 0.01$) of five WDS point analyses.

the minimum detected number of Ir atoms per (Y+La) atoms. The variation of z and x versus $X_{La_2O_3}$ is shown in Figure 7.

Discussion

The experimental results confirm that molten La_2O_3, molten Y_2O_3, and their pseudo binary for the compositions investigated decompose into metallic La and Y, and oxygen under an applied electric field across iridium electrodes. Furthermore, the corresponding half-cell reaction describing the co-reduction of rare earth ions R^{3+} to $\underline{R}(l)$ (here R=La or Y) alloyed with Ir is given by:

$$R^{3+}\,(melt) + 3e^- \rightleftharpoons \underline{R}\,(l) \qquad [7]$$

The state of $\underline{R}(l)$ is considered to be rare-earth metal dissolved in liquid Ir, i.e. the liquidus composition in the ternary Ir-La-Y. Such consideration is inherited from several findings reported herein:

- The similarity of obtained 2nd and higher current harmonic peak-splitting features to that observed for an Ir anode in molten Al_2O_3 (compare $I_{2\omega}$ and $I_{3\omega}$ shown in Figure 2 with those shown in Nakanishi et al.).[12]
- The high REE content of the cathode products following electrolysis at $E < E_C^*$ (Figures 6 and 7).
- Electrolysis at $E > E_C^*$ (less negative), shows no indication of REE-Ir alloy formation, with a content of REE in the Ir cathode below the detection limit of WDS.
- According to our results and the limited thermodynamic data available,[19] the formation of rare earth suboxide gaseous species, is unfavorable.

For a given cell configuration, U^o then represents the minimum cell voltage required to drive Reaction 7 on the cathode while Reaction 6 is occurring on the anode, as presented before for molten aluminum oxide.[12]

Electrochemical production of rare-earth and selectivity.—The observations and analysis of the iridium cathode after galvanostatic electrolysis confirm the feasibility of lanthanum (Figures 6a and 6g) and yttrium (Figures 6f and 6l) electrochemical production from their pure molten oxide at temperature in excess of 2500 K. Rare-earth elements are found alloyed with iridium, leading to melting of the cathode, in agreement with their melting point ($T_{fus}^{La} = 1193$K, $T_{fus}^{Y} = 1799$ K) and prior reports on their phase stability with iridium. The intermetallic $LaIr_2$ found in the microstructure is formed from solidification of a liquid alloy, as exemplified by the solidified eutectic

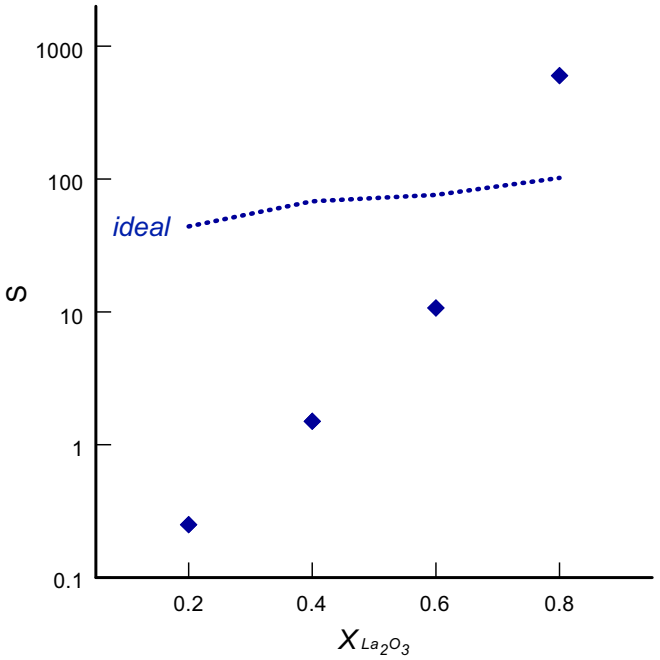

Figure 8. Variation of the experimental selectivity for La recovery in the metal cathode product (Eq. 3, diamonds) as a function of the La_2O_3 content in the electrolyte, compared with the prediction for an ideal mixing in both the electrolyte and the liquid metal cathode (Eq. 5, dashed line, calculated at each temperature).

structure presented in Figure 6g. The results also confirm production of liquid Y (Figures 6f and 6l), though the exact stoichiometry (x) in YIr_x escaped our analytical resolution.

A highly selective recovery of La over Y in the metal cathode (e.g. S=77 at 2585K from Eq. 3), is anticipated from ideal mixing in both the electrolyte and the liquid metal products. Figure 8 compares the experimental selectivity according to Eq. 3 calculated using the average La and Y content measured in the cathode (z in Figure 7) with this ideal situation, for the various electrolyte compositions and estimated temperatures. The predictions assuming ideal mixing in all phases are not compatible with the experimental findings. A greater selectivity for La is found for 20% yttria in the electrolyte, while the selectivity for La decreases drastically above 50% yttria, and becomes marginal (S around 1) at 60%. Enrichment in Y in the metal product is more favored than ideality predicts for yttria content at 80%, with a selectivity for La of 0.25 (resp. 4 for Y). Such finding suggests departure from ideality in the electrolyte as well as potentially in the metal cathode product. The selective enrichment of La in a metal cathode product - with corresponding enrichment in yttrium oxide in the electrolyte with time - is shown to be in principle feasible. The existence of non-ideality also shows the ability to extract the most reactive rare-earth (Y) for concentrations in rare-earth oxide where standard state thermodynamic would predict the opposite, an important finding considering that those elements are typically recovered only after numerous unit operations in existing processes.

Clearly a "continuous" enrichment in a single reactor with continuous removal of the metal product operating with the same initial yttria-poor mixture could be limited only to certain yttrium content in the electrolyte (e.g. at 60% yttria). If similar thermodynamic were to be found for the other rare-earth elements, along with a more affordable cathode host than iridium, the electrolytic approach from molten oxide could offer a new approach for selective concentration of certain rare-earth elements as metal products, or as new concentrate oxide. This could be of future interest for REE extraction from concentrate since La is one of the most abundant elements of the series in several REE concentrates, and Y has very limited market application. Interest could be for elements that are less reactive than both La and Y

at 2585K (e.g. Gd, Pr, Sm), of similar reactivity as La (e.g. Nd) or even almost as reactive as Y (e.g. Dy). Clearly such interest will lie in their respective concentration in the concentrate, and their non-ideal mixing behavior in their molten oxide state. Importantly, the mixing behavior of the electrolyte can also be informed from the individual ACV signals reported herein, as discussed hereafter.

Thermodynamic analysis of molten La_2O_3-Y_2O_3.—The potential of the oxygen evolving anode in La_2O_3-Y_2O_3 is considered fixed during the measurements of U^o assuming:

1. O_2 (g) chemical potential (μ_{O_2}) variation is negligible due to mechanical equilibrium constraints (including surface tension effects) and low vapor pressure of the oxide melt, cf. Table II, and the non-condensed nature or instability of other possible anodic species (e.g. IrO_x).
2. O^{2-} chemical potential ($\mu_{O^{2-}}$) variation is negligible due to charge neutrality constraints and the negligibly small concentrations of Ir observed in the electrolyte.

Oxide inclusions were observed in the cathode deposit following electrolysis near the electrode-electrolyte interface, as shown in Figure 6c with the grey inclusions in the white, metallic cathode. This situation is possible in two foreseeable scenarios:

1. The liquid alloy product exhibits high solubility for molecular O, which was transported to the cathode from the furnace atmosphere via the melt and/or via the triple-phase boundary (Ir cathode-molten droplet-furnace gas), and reacted with REE present in the alloy liquid to form the oxide inclusions during solidification upon quenching.
2. During deposition or solidification, the electrolyte became entrapped in a "mushy" (both solid and liquid alloy phases present) cathode deposit.

If the latter scenario was operating, then the ternary alloy liquid Ir-La-Y is the relevant system for further thermodynamic analysis. However, if the former occurred, then the Ir-La-Y-O quaternary system is relevant and interactions between La-Y-O in the Ir solvent require further consideration for the thermodynamic analysis. Data for Ir-La-Y-O system, especially, the Ir-rich region are not available at present.[20–24] However, analyses for both scenari reduce to identical thermodynamic formalisms in the limit of infinite dilution. Given that La, Y and O concentrations are expected to be small at the liquidus phase boundary (the WDS analysis showed very small O content in the solidified liquid metal phases), the behavior of these species is treated as infinite dilution in an Ir liquid solvent.

For the pseudo-unary electrolytes (i.e. $X_{La_2O_3} = 0$ and 1), the thermodynamic analysis proceeds in a similar fashion to that described in Nakanishi et al.[16] That is, U^o is the decomposition voltage for the overall cell reaction 1. The corresponding Gibbs energy change may be computed via:

$$\Delta_r G = 6FU^o = 2\mu_{M(l)} + 1.5\mu^o_{o_2} - \mu^o_{M_2O_3} \quad [8]$$

where $\mu^o_{O_2}$ and $\mu^o_{M_2O_3}$ are the standard chemical potentials of O_2 (g) and M_2O_3 (l), resp. (for both, standard states pure species at temperature T and $p = 101{,}325$ Pa). The decomposition voltage U^o for Reaction 1 for other compositions in the pseudo-binary La_2O_3-Y_2O_3 is also related to the corresponding Gibbs energy change as similarly evaluated in Eq. 8

$$\Delta_r G = 6FU^o = 2\mu_{M(l)} + 1.5\mu^o_{o_2} - \mu_{M_2O_3} \quad [9]$$

where $\mu_{M_2O_3}$ is equivalent, under the given assumptions, to the equilibrium chemical potential of M_2O_3 (l) in the bulk La_2O_3-Y_2O_3 melt. The variation of $\mu_{M_2O_3}$ with $X_{M_2O_3}$ can be expressed as:

$$\mu_{M_2O_3} = \mu^o_{M_2O_3} + RT \ln \gamma_{M_2O_3} + RT \ln X_{M_2O_3} \quad [10]$$

where $\gamma_{R_2O_3}$ is the activity coefficient for M_2O_3 (l). Rearranging Eq. 10 and combining with Eq. 8 yields an expression for the partial molar excess Gibbs energy of M_2O_3 (l):

$$G^E_{M_2O_3} \equiv RT\ln\gamma_{M_2O_3} = 2\mu_M + \frac{3}{2}\mu^o_{O_2} - 6FU^o - \mu^o_{M_2O_3} - RT\ln X_{M_2O_3} \quad [11]$$

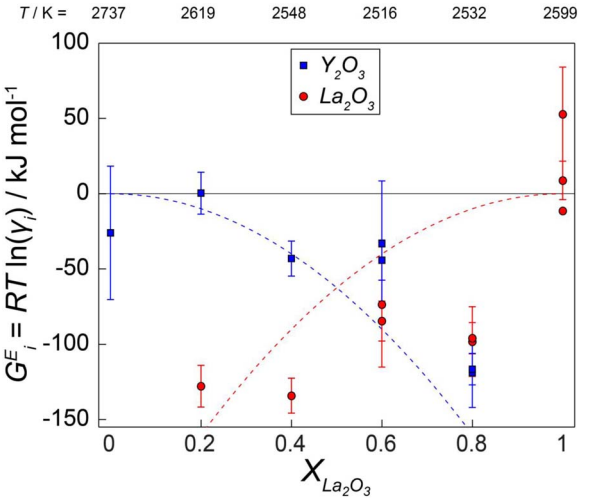

Figure 9. Variation of the partial molar excess Gibbs energy (G^E_i) for i = La_2O_3 (red circles) or Y_2O_3 (blue squares) with $X_{La_2O_3}$ for the pseudo-binary La_2O_3-Y_2O_3 liquid (standard state pure liquid La_2O_3 or Y_2O_3 at temperature T). Dashed lines correspond to G^E_i for a hypothetical regular solution with model parameter $\omega_{ij} = -50$ kJ mol^{-1}. For $X_{La_2O_3} = 0$ and 1, G^E_i represents the difference between measured and assessed molar Gibbs energies for the pure components ($\mu^o_{i,meas.} - \mu^o_{i,tab.}$).

Decomposition potential results U^o are provided in Figure 4, and $\mu^o_{O_2}$ is tabulated.[25] The next step in order to further inform the thermodynamic for the pure and pseudo-binary molten oxides ($\mu^o_{M_2O_3}$ in Eq. 8 and $\mu_{M_2O_3}$ in Eq. 9) relies on information about the chemical potential μ_M of the metals in the cathode; as detailed in Appendix 1. Therein, the chemical potential of M (= La, Y) is evaluated at the liquidus composition of the M-Ir binary alloy.

The temperatures for each composition shown in Table III are based upon a 25 K superheat above an average of the experimentally determined La_2O_3-Y_2O_3 liquidus temperatures.[13,26] The accepted value for $T^{Ir}_{fus} = 2719$K[27,28] then conflicts with the operating temperature found here for pure Y_2O_3 ($T = T^{Y_2O_3}_{fus} + 25\,\text{K} = 2737\,\text{K}$), as no melting was observed during non-polarized contact between Ir and pure molten Y_2O_3 in our experiments. Henning et al.[28] reported the most recent measurement of T^{Ir}_{fus} in year 1933. $T^{Y_2O_3}_{fus}$ was determined by an international collaboration involving ten laboratories and was found to be invariant with atmosphere.[29] Given the accuracy of the recently reported measurements for La_2O_3,[30] the assessed data for $\mu^o_{La_2O_3}$ combined with the present results were used to determine T^{Ir}_{fus}. An agreement between tabulated and measured $\mu^o_{La_2O_3}$ was found for $T^{Ir}_{fus} = 2769$ K, which is 50 K above the value reported by Henning et al.[28] Perhaps, low purity specimens employed in 1933 in Reference 28 contributed to the discrepancy at the time.

Previously optimized thermodynamic descriptions are available for $\mu^o_{La_2O_3}$ and $\mu^o_{Y_2O_3}$.[30–35] Chen et al.[32] also incorporated the previous optimizations of La-O[33] and Y-O.[34] The description by Chen et al.[32] for $\mu^o_{Y_2O_3}$ was herein updated with the more recent measurements by Ushakov et al.[30] (data provided in Table II). For $X_{La_2O_3} = 0$ and 1, Figure 9 shows the difference between measured and assessed molar Gibbs energies for the pure components ($\mu^o_{i,meas.} - \mu^o_{i,tab.}$). The measured $\mu^o_{Y_2O_3}$ was approximately 50 kJ mol^{-1} higher than the assessed value by Chen et al.[32] The result for $\mu^o_{Y_2O_3}$ was very sensitive to T^{Ir}_{fus}. A more accurate determination of T^{Ir}_{fus} and the development of a method for in situ measurement of absolute temperature, would improve interpretation of the results for the end members, $\mu^o_{La_2O_3}$ and $\mu^o_{Y_2O_3}$. For

intermediate compositions, and despite the scattering of some data points and difficulty repeating measurements at $X_{La_2O_3} = 0.4$, the analysis presented in Figure 9 suggests negative deviation from ideality for the molten La_2O_3-Y_2O_3, in qualitative agreement with the departure from an ideal selectivity for La.

Critical assessment and recommendation.—Before drawing further conclusions about the La_2O_3-Y_2O_3 mixing behavior, a discussion on the possible error introduced by the thermodynamic model used for liquid La-Ir-Y (presented in Appendix 1) is warranted. La and Y were assumed to behave as infinitely dilute solutes in Ir. At the minimum temperature investigated ($T \approx 2516$ K), the liquidus composition approaches $X_{\underline{R}} \approx 0.16$ (assuming Equation A2 is valid), which brings to question the assumption of Henrian behavior of La-Y as solutes for the lower melting intermediate composition. As the concentration for La measured during the electrolysis experiments and Y are increased, the activity coefficient ($\gamma_{\underline{R}}$) is expected to increase towards unity. Therefore, $G^E_{R_2O_3}$ is expected to increase (become more positive) at the intermediate concentrations as $RT \ln \frac{\gamma_{\underline{R}}}{\gamma^{\infty}_{\underline{R}}}$. Additionally, the excess entropy at infinite dilution ($\Delta S_i^{E,\infty}$) was assumed to be negligibly small for the La-Ir-Y liquid alloy. At such high temperature though, even minor entropic effects contribute significantly to the Gibbs energy, possibly invalidating this assumption. The central atom model and its modifications[36–38] predict $\Delta S_i^{E,\infty} = \frac{\Delta H_i^{\infty}}{\tau}$, where τ is an empirical constant with a value of 2500 ± 1000 K for binary substitutional alloys. $\Delta S_i^{E,\infty}$ and ΔH_i^{∞} have generally be observed to share sign. Therefore, for the strong REE-Ir interactions present ($\Delta H_i^{\infty} \ll 0$), a non-negligible $-T\Delta S_i^{E,\infty}$ contribution to $\mu_{\underline{R}}$ would effectively increase $G^E_{R_2O_3}$ at all compositions and most significantly near the end-member compositions where operating temperature is greatest. However, previous semi-empirical correlations[36–38] do not include data for interactions between platinum group metals (Ir, Pt, etc.) and Group III metals (Sc, Y, La, etc.), which tend to form very stable intermetallic compounds with relatively small formation entropies.[39] Therefore, the present assumption $\Delta S_i^{E,\infty} = 0$ appears justified given the available data and prior art. Nevertheless, an improved description of the La-Y-Ir system (i.e. study of T^{Ir}_{fus}, description for the ternary liquidus phase boundary, activity coefficients for La and Y in Ir-rich liquid alloy) would significantly benefit interpretation of the present results.

The presence of dissolved molecular oxygen in the alloy liquid was neglected, but its possible role in affecting the mixing properties of La_2O_3-Y_2O_3 can be discussed. The oxide inclusions found in the deposit near the electrolyte indicate that oxygen may have been present at non-negligible concentrations in the liquid alloy, though its solubility would have then drastically decreased upon solidification. The parameter z was measured at the center of the electrode far away from the electrolyte and oxide inclusions, in an effort to minimize influence of the preferential back reaction to form Y_2O_3 on the observed z. If oxygen was indeed present in the liquid Ir, it would increase parameter z, which would in turn increase (make more positive) $\mu_{\underline{La}}$ and $G^E_{La_2O_3}$ and decrease μ_Y and $G^E_{Y_2O_3}$ at a given composition. Therefore, interactions of Y and La with oxygen could account for the relative spacing between $G^E_{La_2O_3}$ and $G^E_{Y_2O_3}$ values, which is more predominant at high $X_{Y_2O_3}$ (higher Y content in the deposit). Nevertheless, the importance of this feature could be mitigated or investigated by employing methods limiting electrolyte back reaction such as using a higher quench rate or repeating measurements in a more reducing atmosphere, i.e. at a lower oxygen fugacity.

Dispersion of Ir from the anode was observed. The presence of Ir ions in the melt may have influenced the activity of oxide ions in the melt at the surface of the anode, thus altering the inner potential of the anode during measurement of U^o. Given the remarkably close agreement between measured and tabulated data for $\mu^o_{La_2O_3}$ and $\mu^o_{Y_2O_3}$, and the low concentrations observed for Ir in the electrolyte, this feature is not anticipated to have significant influence on the results. Clearly, further investigation of Ir inertness (i.e. studies at different temperatures and oxygen partial pressures) may be necessary for process development, as well as to provide further insights on the significance of this effect on the measured thermodynamic properties.

Conclusions

For the first time, La_2O_3, Y_2O_3 and their mixture were electrolytically decomposed using Ir wires, confirming the electrolytic nature for these melts and ability to extract rare-earth elements. Oxygen gas evolution was observed at the anode and La and Y were observed to co-deposit for the La_2O_3-Y_2O_3 mixtures investigated. Selective extraction of La was observed for $X_{La_2O_3} > 0.2$. Post-experiment observations indicated a liquid alloy phase forms at the cathode surface for $U > U(E^*_C)$.

The method for decomposition voltage measurement described previously for Al_2O_3 was applied to the pseudo-binary system La_2O_3-Y_2O_3. The results indicate that molten La_2O_3-Y_2O_3 is not an ideal mixture, contradicting previous predictions. Further considerations suggest that the present thermodynamic analysis would benefit from:

- an improved thermodynamic model for the metallic alloy La-Y-Ir, taking into account the non-dilute mixing behavior of La and Y
- a means of eliminating or accounting for the back reaction between Y and La and dissolved oxygen in the cathode to improve reliability of parameter z

An improved thermodynamic model and removal of the influence of dissolved oxygen could explain the discrepancies between the measured data and those predicted previously for La_2O_3-Y_2O_3. However, given the observed variation in the selective extraction of La and Y from La_2O_3-Y_2O_3, ideal mixing for molten La_2O_3-Y_2O_3 appears to be inaccurate. The selective enrichment observed here, if shown to extend to other REE and REO systems, suggests a possible new approach for direct, selective, REE separation and recovery directly from mixed oxides.

Acknowledgments

The authors gratefully acknowledge the experimental contributions from Melody Wang, Erick I. Hernandez and the thermodynamic insights from Mary-Elizabeth Wagner. This research was funded by the US Office of Naval Research (ONR) under grant Contract # N00014-11-1-0657.

Appendix

Decomposition cell voltage analysis is proposed with the following simplifying assumptions:

1. Given the relatively low concentrations of REE deposited in Ir and high concentrations of La and Y in the oxide phase, the variation in $\mu_{R_2O_3}$ is negligible during an experiment. A more detailed analysis explaining the pertinence of such assumption can be found in Kawamura et al.[40,41]
2. Relative proportions of La and Y in liquid Ir-La-Y alloy are hypothesized to be precisely that of parameter z shown in Figure 7, i.e. z observed in the quenched droplet following electrolysis at $U > U^o$ is equivalent to the relative proportions of La and Y near the cathode-electrolyte interface at $U^o = U(E^*_C)$.

Thermodynamic data for the Ir-La-Y system, especially in the Ir-rich, high temperature portion of state variable space, are severely lacking.[20–24] Therefore, a thermodynamic model for μ_R was developed using the following assumptions:

1. The standard states for all species in the liquid alloy phase are of their own pure liquids at T, $p = 101{,}325$ Pa.
2. La and Y behave as infinitely dilute solutes in an Ir liquid solvent. La and Y chemical interactions with themselves in the liquid are negligible in comparison to interactions with the Ir solvent.
3. The solubility of La and Y in Ir (s) is negligibly small. This assumption is supported by experimental observations of Y solubility in Ir (< 0.1 at%, detection limit of field emission electron probe micro-analysis equipment employed) following annealing at 1973 K for 100 h.[23] No similar studies on La-Ir have been reported to the author's knowledge.

4. The composition of the liquidus for the R-Ir pseudo-binary (X_{Ir}^{l}) is described by the expression:[42]

$$\ln\left(X_{Ir}^{l}\right) = -\frac{\Delta_{fus}H_{Ir}^{o}}{R}\left(\frac{1}{T} - \frac{1}{T_{fus,Ir}}\right) \quad [A1]$$

where $\Delta_{fus}H_{Ir}^{o}$ (= 41.14 kJ mol^{-1}[43]) and $T_{fus,Ir}$ (discussed below) are the melting enthalpy and temperature, resp., for pure Ir.

5. The partial molar excess Gibbs energy of La and Y in Ir obeys the expression

$$G_i^E = RT\ln\gamma_i^{\infty} = \Delta H_i^{\infty} - T\Delta S_i^{E,\infty} \quad [A2]$$

where γ_i^{∞}, ΔH_i^{∞} and $\Delta S_i^{E,\infty}$ are the Henrian coefficient and partial molar excess enthalpy and entropy for species i at infinite dilution in Ir liquid, resp.

6. The semi-empirical Miedema model[44] accurately describes ΔH_i^{∞} for $i = (La, Y)$ in Ir (l) ($\Delta H_{La}^{\infty} = -230$ kJ mol^{-1} and $\Delta H_{Y}^{\infty} = -242$ kJ mol^{-1})
7. The excess partial molar entropy for La or Y is $\Delta S_i^{E,\infty} = 0$

The preceding assumptions permit determination of μ_M for a given T according to

$$\mu_M = \mu_M + RT\ln X_M + RT\ln\gamma_M^{\infty} \quad [A3]$$

where $RT\ln\gamma_M^{\infty}$ is given by Eq. A2; $X_{La} = z(1 - X_{Ir}^{l})$ and $X_Y = (1 - z)(1 - X_{Ir}^{l})$ where X_{Ir}^{l} is given by Eq. A1.

The results for $RT\ln\gamma_{R_2O_3}$ variation with $X_{La_2O_3}$ are presented in Figure 4.

ORCID

Antoine Allanore https://orcid.org/0000-0002-2594-0264

References

1. S. M. Bennett, "2015 Minerals Yearbook," *United States Geol. Surv.*, no. September, p. 14 (2018).
2. K. Binnemans, P. T. Jones, K. Van Acker, B. Blanpain, B. Mishra, and D. Apelian, "Rare-Earth Economics: The Balance Problem," *JOM*, **65**(7), 846 (2013).
3. F. Xie, T. A. Zhang, D. Dreisinger, and F. Doyle, "A critical review on solvent extraction of rare earths from aqueous solutions," *Miner. Eng.*, **56**, 10 (2014).
4. Y. B. Aba, F. K. Ubota, N. K. Amiya, and M. G. Oto, "Recent Advances in Extraction and Separation of Rare-Earth Metals Using Ionic Liquids," *J. Chem. Eng. Japan*, **44**(10), 679 (2011).
5. G. Adachi, *Science of Rare Earths*. Kyoto: Kagakudojin, (1999).
6. F. Xie, T. A. Zhang, D. Dreisinger, and F. Doyle, "A critical review on solvent extraction of rare earths from aqueous solutions," *Miner. Eng.*, **56**, 10 (2014).
7. C. K. Gupta and N. Krishnamurthy, "Extractive Metallurgy of Rare Earths," vol. **m** (2005).
8. T. Uda, "Technique for Enhanced Rare Earth Separation," *Science (80-.).*, **289**(5488), 2326 (2000).
9. C. K. Gupta and N. Krishnamurthy, *Extractive Metallurgy of Rare Earths*, New York: CRC Press, (2004).
10. J. P. Ackerman and J. L. Settle, "Distribution of plutonium, americium, and several rare earth fission product elements between liquid cadmium and LiClKCl eutectic," *J. Alloys Compd.*, **199**(1–2), 77 (1993).
11. E. C. Slater, Raraz S. A., Willit A. G., and Gay J., "Electrochemical Separation of Aluminum from Uranium for Research Reactor Spent Nuclear Fuel Applications," *Sep. Purif. Technol.*, **15**(3), 197 (1999).
12. B. R. Nakanishi and A. Allanore, "Electrochemical study of a pendant molten alumina droplet and its application for thermodynamic property measurements of Al-Ir," *J. Electrochem. Soc.*, **164**(13), E460 (2017).
13. L. M. Lopato, B. S. Nigmanov, A. V. Shevchenko, and Z. A. Zaitseva, "Interaction Between Lanthanum Oxide and Yttrium Oxide (Translation)," *Neorg. Mater.*, **22**(5), 771 (1984).
14. J. Coutures and M. Foex, "Etude a Haute Temperature du Diagramme d'Equilibre du Systeme Forme par le Sesquioxyde de Lanthane avec le Sesquioxyde d'Yttrium," *J. Solid State Chem.*, **11**, 294 (1974).
15. M. Mizuno, A. Rouanet, T. Yamada, and T. Noguchi, "Phase diagram of the system La2O3-Y2O3 at high temperatures," *Yogyo-Kyokai-Shi*, **84**(7), 342 (1976).
16. B. R. Nakanishi and A. Allanore, "Electrochemical study of a pendant molten alumina droplet and its application for thermodynamic property measurements of Al-Ir," *J. Electrochem. Soc.*, **164**(13), E460 (2017).
17. S. Sokhanvaran, S.-K. Lee, G. Lambotte, and A. Allanore, "Electrochemistry of molten sulfides: copper extraction from BaS-Cu2S," *J. Electrochem. Soc.*, **163**(3), D115 (2016).
18. H. Kim, J. Paramore, A. Allanore, and D. R. Sadoway, "Stability of Iridium Anode in Molten Oxide Electrolysis for Ironmaking: Influence of Slag Basicity," in *Electrochemical Society Transactions*, 2010, **33**(7), 219.
19. C. W. Bale et al., "FactSage thermochemical software and databases, 2015," *CALPHAD Comput. Coupling Phase Diagrams Thermochem.*, **54**, 35 (2016).
20. H. Okamoto, "The Ir-La (Iridium-Lanthanum) System," *J. Phase Equilibria*, **12**(5), 565 (1991).
21. H. Okamoto, "The Ir-Y (Iridium-Yttrium) system," *Phase Diagr. Eval.*, **13**(6), 651 (1992).
22. K. T. Jacob, T. H. Okabe, T. Uda, and Y. Waseda, "Solid-state cells with buffer electrodes for accurate thermodynamic measurements: System Nd-Ir-O," *Electrochim. Acta*, **45**(12), 1963 (2000).
23. N. Sekido, H. Murakami, and Y. Yamabe-Mitarai, "Phase equilibria and oxidation behavior of Ir-rich Ir-Y binary alloys," *J. Alloys Compd.*, **476**(1–2), 107 (2009).
24. H. Okamoto, "Supplemental literature review of binary phase diagrams: Ag-Nd, Ag-Zr, Al-Nb, B-Re, B-Si, In-Pt, Ir-Y, Na-Si, Na-Zn, Nb-P, Nd-Pt, and Th-Zr," *J. Phase Equilibria Diffus.*, **35**(5), 636 (2014).
25. D. R. Stull and H. Prophet, "JANAF thermochemical tables," *J. Phys. Chem. Ref. Data*, (1985).
26. J. Coutures, F. Sibieude, and M. Foex, "Etude a Haute Temperature des Systemes Formes par Les sesquioxydes de Lanthane Avec les Sesquioxydes de Lanthanides II . Influence de la Trempe sur la Nature des Phases Obtenues a la Temperature Ambiante," *J. Solid State Chem.*, **17**, 377 (1976).
27. R. E. Bedford, G. Bonnier, H. Maas, and F. Pavese, "Recommended values of temperature on the International Temperature Scale of 1990 for a selected set of secondary reference points," *Metrologia*, **33**, 133 (1996).
28. F. Henning and H. T. Wensel, "The freezing point of iridium," *Bur. Stand. J. Res.*, **10**(6), 809 (1933).
29. J. Hlavac, "Melting temperatures of refractory oxides: Part I," *Pure Appl. Chem.*, **54**(3), 681, (1982).
30. S. V. Ushakov and A. Navrotsky, "Direct measurements of fusion and phase transition enthalpies in lanthanum oxide," *J. Mater. Res.*, **26**(07), 845 (2011).
31. M. Zinkevich, "Thermodynamics of rare earth sesquioxides," *Prog. Mater. Sci.*, **52**(4), 597 (2007).
32. M. Chen, B. Hallstedt, and L. J. Gauckler, "CALPHAD modeling of the La2O3-Y2O3 system," *CALPHAD Comput. Coupling Phase Diagrams Thermochem.*, **29**(2), 103 (2005).
33. A. N. Grundy, B. Hallstedt, and L. J. Gauckler, "Thermodynamic assessment of the lanthanum-oxygen system," *J. Phase Equilibria*, **22**(2), 105, (2001).
34. V. Swamy, H. J. Seifert, and F. Aldinger, "Thermodynamic properties of Y2O3 phases and the yttrium-oxygen phase diagram," *J. Alloys Compd.*, **269**(1–2), 201 (1998).
35. P. Wu and A. D. Pelton, "Coupled thermodynamic phase diagram assessment of the rare earth oxide aluminum oxide binary systems," *J. Alloys Compd.*, **179**, 259 (1992).
36. C. H. . Lupis and J. . Elliott, "Prediction of enthalpy and entropy interaction coefficients by the 'central atoms' theory," *Acta Met.*, **15**(2), 265 (1967).
37. T. Tanaka, N. A. Gokcen, and Z. Morita, "Relationship between enthalpy of mixing and excess entropy in liquid binary alloys," *Zeitschrift fuer Met.*, **81**(1), 49 (1990).
38. T. Tanaka, N. A. Gokcen, and Z. Morita, "Relationship between partial enthalpy of mixing and partial excess entropy of solute elements in infinitely dilute solutions of liquid binary alloys," *Zeitschrift für Met.*, **81**(5), 349 (1990).
39. L. Brewer and P. R. Wengert, "Transition metal alloys of extraordinary stability; An example of generalized Lewis-acid-base interactions in metallic systems," *Metall. Trans.*, **4**(1), 83 (1973).
40. A. Sasahira, K. Kawamura, M. Shimizu, N. Takada, M. Hongo, and T. Yokokawa, "Pb2+/Pb0 Redox Equilibria in Sodium Borate, Silicate, and Aluminosilicate Melts," *J. Electrochem. Soc.*, **136**(7), 1861 (1989).
41. K. Kawamura and T. Yokokawa, "Linear sweep voltammetry of Pb2+/Pb in oxide melts," *J. Electrochem. Soc.*, **135**(6), 1447 (1988).
42. C. H. P. Lupis, *Chemical Thermodynamics of Materials*. New York: North-Holland (1983).
43. A. T. Dinsdale, "SGTE data for pure elements," *CALPHAD Comput. Coupling Phase Diagrams Thermochem.*, **15**(4), 317 (1991).
44. F. R. de Boer, R. Boom, W. C. M. Mattens, A. R. Miedema, and A. K. Niessen, *Cohesion in Metals: Transition Metal Alloys*. New York: North-Holland (1988).
45. S. V. Ushakov and A. Navrotsky, "Experimental Approaches to the Thermodynamics of Ceramics Above 1500°C," *J. Am. Ceram. Soc.*, **95**(5), 1463 (2012).
46. J. Hlavac, "Melting temperatures of refractory oxides: Part I," *Pure Appl. Chem.*, **54**(3) (1982).
47. M. Zinkevich, "Thermodynamics of rare earth sesquioxides," *Prog. Mater. Sci.*, **52**(4), 597 (2007).
48. E. E. Shpil'rain, D. N. Kagan, L. S. Barkhatov, and V. V. Koroleve, "Measurement of the enthalpy of solid and liquid phases of yttria," *High Temp. - , High Press.*, **8**, 183 (1976).
49. B. Granier and S. Heurtault, "Density of Liquid Rare-Earth Sesquioxides," *J. Am. Ceram. Soc.*, **71**(11), 466 (1988).
50. C. W. Bale et al., "FactSage thermochemical software and databases, 2015," *CALPHAD Comput. Coupling Phase Diagrams Thermochem.*, **54**, 35 (2016).
51. E. E. Shpil'rain, D. N. Kagan, L. S. Barkhatov, and L. I. Zhmakin, "Electrical conductivity of yttrium and scandium oxides," *Rev. Int. Hautes Temper. Refract.*, **16**(3), 233 (1979).
52. A. Jain et al., "Commentary: The materials project: A materials genome approach to accelerating materials innovation," *APL Mater.*, **1**(1) (2013).
53. J. Coutures, A. Rouanet, R. Verges, and M. Foex, "Etude a Haute Temperature des Systemes Formes par le Sesquioxyde de Lanthane et les Sesquioxydes de Lanthanides. I. Diagrammes de Phases (1400°C < T < T Liquide)," *J. Solid State Chem.*, **17**, 171 (1976).
54. S. V. Ushakov and A. Navrotsky, "Direct measurements of fusion and phase transition enthalpies in lanthanum oxide," *J. Mater. Res.*, **26** (07), 845 (2011).